

# LoRa Backscatter Communications: Temporal, Spectral, and Error Performance Analysis

Ganghui Lin, *Graduate Student Member, IEEE* Ahmed Elzanaty, *Senior Member, IEEE*, and Mohamed-Slim Alouini, *Fellow, IEEE*

**Abstract**—LoRa backscatter (LB) communication systems can be considered as a potential candidate for ultra low power wide area networks (LPWAN) because of their low cost and low power consumption. In this paper, we comprehensively analyze LB modulation from various aspects, i.e., temporal, spectral, and error performance characteristics. First, we propose a signal model for LB signals that accounts for the limited number of loads in the tag. Then, we investigate the spectral properties of LB signals, obtaining a closed-form expression for the power spectrum. Finally, we derived the symbol error rate (SER) of LB with two decoders, i.e., the maximum likelihood (ML) and fast Fourier transform (FFT) decoders, in both additive white Gaussian noise (AWGN) and double Nakagami-m fading channels. The spectral analysis shows that out-of-band emissions for LB satisfy the European Telecommunications Standards Institute (ETSI) regulation only when considering a relatively large number of loads. For the error performance, unlike conventional LoRa, the FFT decoder is not optimal. Nevertheless, the ML decoder can achieve a performance similar to conventional LoRa with a moderate number of loads.

**Index Terms**—symbol error rate (SER); LoRa backscatter (LB); Internet of Things (IoT); power spectral density

## I. INTRODUCTION

The goal of 5G and beyond networks is to realize three core services, i.e., enhanced mobile broadband (eMBB), ultra reliable low latency communications (URLLC), and massive machine type communications (mMTC) [1], [2], to support extreme network capacity, latency-sensitive critical missions, and a massive number of connected devices, respectively. In mMTC, a colossal variety of inexpensive devices is needed to communicate at low power consumption. With nearly 30 billion devices expected to be connected by 2030 [3], the prospect of mMTC makes it possible for Internet of Things (IoT) applications such as smart cities, homes, and agriculture.

In this regard, many wireless technologies have recently emerged to realize such low-power communications with low-priced devices. For instance, low power long range wide area network (LoRaWAN), SigFox, and narrowband Internet of things (NB-IoT) are three prominent technologies supporting low power wide area networks (LPWAN) [4]–[7]. However,

some application scenarios put forward more stringent requirements on the power consumption that even technologies such as LPWAN cannot meet.

In this context, backscatter communication (BC) is one of the most remarkable technologies for ultra-low-power communications with its ability to operate with sub-milliwatt power consumption. Typical BC systems contain backscatter tags and transceivers. The tag reflects the incoming excitation signals while modulating it with its data by changing the incident signal amplitude, frequency, or phase [8]. The innovation of BC lies in its radio-passive property that removes the power-consuming analog components such as RF oscillators, decoupling capacitors, and crystals. Hence, BC devices can operate with emerging flexible and printed batteries or even harvest environmental energy [9], [10].

BC can be divided into three categories based on the adopted architecture: (i) *monostatic backscatter*, where a tag modulates an excitation signal generated by a transceiver, then reflects it back to the transceiver; (ii) *bistatic backscatter*, where the transmitter (Tx) and receiver (Rx) are separated; (iii) *ambient backscatter*, where the excitation signal comes from existing surrounding RF sources in the environment [11], [12].

Despite the low-cost, low-power merits that BC owns, one of the most detrimental defects of BC is its limited communication range. The electromagnetic waves suffer from severe multipath fading and strong attenuation in urban or indoor environments, significantly reducing the coverage of BC [13]. In some medical or wearable applications, the human body also shortens the communication range [14].

One possible solution to this problem is LoRa backscatter (LB), where the backscatter tag generates chirp spread spectrum (CSS) modulated signals to improve the robustness of BC [15]. LoRa modulated signals have exceptionally high sensitivity up to  $-149$  dBm, compensating for the long-range path loss as well as the multipath fading effects. Although LB is similar, to some extent, to LoRa modulation in terms of high sensitivity, they differ in many aspects. First, the LB modulated signals only have a finite number of phases because of the limited number of antenna loads in the backscatter tags. Second, conventional LoRa Tx's are active devices that directly transmit signals to the gateway, hopefully through a line of sight link. In contrast, in LB the signals from the Tx pass through the channel between the Tx and tag before backscattered to the Rx, i.e., double-fading channel.

The aforementioned aspects make a huge difference in analyzing the performance of LB. More precisely, a double fading channel should be considered in LB, resulting in

Ganghui Lin and Mohamed-Slim Alouini are with the Division of Computer, Electrical and Mathematical Sciences and Engineering, King Abdullah University of Science and Technology, Thuwal 23955-6900, Saudi Arabia (e-mail: ganghui.lin@kaust.edu.sa, slim.alouini@kaust.edu.sa).

A. Elzanaty is with the 5GIC & 6GIC, Institute for Communication Systems (ICS), University of Surrey, Guildford, GU2 7XH, United Kingdom (e-mail: a.elzanaty@surrey.ac.uk).

The source codes can be accessed at <https://github.com/SlinGovie/LoRa-Backscatter-Performance-Analysis>.

a more complicated probability density function (PDF) for the channel amplitude. The discrete phases also make the waveforms representing different symbols non-orthogonal at the Nyquist sampling rate, rendering non-equivalency between the maximum likelihood (ML) and fast Fourier transform (FFT) decoders.

#### A. Related work

In the following, we review the state-of-the-art LB schemes and the performance analysis regarding BC and LoRa as well as LB.

1) *The State-of-the-art of LB*: In order to increase the range for BC, a LB communication system with a harmonic cancellation scheme is proposed in [15]. The proposed system consists of a single-tone carrier Tx, a backscatter tag, and a Rx. The tag uses the single tone to synthesize CSS modulated signals and reflect them to the Rx. To avoid interference from the RF source, a frequency shift is introduced in the tag by multiplying the incoming signals by an approximated cosine and sine with discontinuous step transitions, resulting in high-frequency components, i.e., the harmonics. The harmonic cancellation is achieved by adding more voltage levels, i.e., more antenna loads in the tag, to better approximate a pure sinusoid. The design presents a reliable wide area network coverage, i.e., 475 m from the Tx and Rx, provided by a low-cost device that consumes 1000x lower power than a normal LoRa Tx. However, the tag still needs a battery as the power source rather than harvesting energy from the environment. In [16], an RF energy harvesting (RFEH) LB scheme is proposed. It is reported that the tag can self-start up while harvesting RF energy from the excitation signal as low as  $-22.5$  dBm and send the acquired data to a Rx that is 381 m away. There are two possible reasons for the shorter range compared to [15]. One is that the RFEH LoRa tag only uses two antenna loads, resulting in more harmonics. Another reason is that the RFEH LoRa tag harvest energy from the RF source instead of having an embedded battery so that a proportion of the energy is used to power the IC. To resolve the problem of deployment difficulties of traditional half-duplex LB, the first full-duplex LB architecture is proposed in [17]. Nevertheless, the full-duplex LB achieves a shorter range due to a different sensitivity protocol and a reduced link budget introduced by a hybrid coupler architecture used to reduce cost.

The above-mentioned LB systems all use single-tone carriers and the tag modulates its bits into a subcarrier to generate LoRa packets. However, there are other LB systems that use normal LoRa modulated waves as excitation signals [18]–[22]. These ambient backscatter designs use simpler modulation methods such as ON-OFF Keying (OOK), which leads to less complicated tag design at a cost of either shorter communication range, more complicated decoding algorithms, or lower throughput.

2) *Performance Analysis for BC, LoRa, and LB*: For BC, several works have considered its performance analysis in terms of detection schemes, error rate, and information rate. In [23], the authors consider frequency shift keying (FSK) with a coherent receiver for the bistatic backscatter radio channel.

Nevertheless, coherent detection is complex and requires channel state information (CSI) estimation. To avoid this difficulty, non-coherent detection schemes for ambient BC have been considered in [24]–[26]. With the different detection schemes mentioned above, the exact bit error rate (BER) for the ambient backscatter system is derived in [25]. Since it uses unknown ambient signals as carriers, the actual capacity is of interest. In [26], the achievable rate of the ambient BC system is analyzed under different channels. Although the performance analysis of several BC systems with conventional modulation schemes (e.g., binary phase shift keying (BPSK), FSK, OOK) have been analyzed in the literature, few works consider long-range CSS modulation such as LB. In the following, we first discuss the performance analysis of conventional LoRa then LB.

For conventional LoRa, the power spectrum characteristics of normal LoRa are analyzed in terms of the Fresnel functions [4], in which the derived expressions are not applicable for LB because of its limited number of phases. In [27], the BER of LoRa in an additive white Gaussian noise (AWGN) channel is derived by using the Monte-Carlo approximation, but the method requires lots of computing resources. The exact symbol error rate (SER) of orthogonal signaling with non-coherent detection is presented in [28, eq: 4.5-44], which is applicable for LoRa. However, the equation is only derived in an AWGN scenario and the high-order combination involved in the equation will introduce severe numerical problems. The exact SER of LoRa modulation in various fading scenarios, i.e., Rayleigh, Rician, and Nakagami fading channels, are analyzed in [29]. Nevertheless, the expressions are hardly computable because of the remaining high-order combination. In [30], simple asymptotic BER expressions of LoRa modulation over Rician and Rayleigh channels are derived at cost of accuracy. The numerical results show poor accuracy at low signal-to-noise ratio (SNR). In [31], an accurate closed-form approximation of the BER in both AWGN and Rayleigh fading channels is derived. However, the analysis for other fading models such as Rician and Nakagami-m fading channels is not included. In [32], the author proposed a new approach based on the Marcum function to estimate the BER of LoRa in different propagation environments, namely, AWGN, Rayleigh, Rician, and Nakagami channels. In [33], a modification of a union bound on the error probability is proposed to calculate the BER with less complexity. The approximation is applicable for both coherent and non-coherent detection. The theoretical performance analysis is also extended to Hamming-coded LoRa systems. In [34], a novel modulation scheme is introduced that employs both up-chirp and down-chirp simultaneously, and its BER is derived in the AWGN channel. Numerical results demonstrate that this scheme achieves a doubled throughput without a significant increase in BER. Further scenarios have been studied such as channel coding [35], interference channels [36], [37], and imperfect orthogonality [38], [39] for LoRa. Although the performance analysis of conventional LoRa modulation over AWGN and various fading channels have been extensively studied in the literature, they do not consider the double fading channel and the limited number of loads that characterize LB.

In [40], the error performance of LB is discussed in AWGN

channels. However, the essential characteristics of LB for the signal model are not considered. For instance, the fact that LB modulated signals only have limited available phases is not considered. Also, since the performance was only in an AWGN channel, it does not account for the double-fading effects which are crucial for LB.

### B. Contributions

Although some prototypes have proved the feasibility of LB, more theoretical insights are needed in order to support the design and deployment of LB systems. Nevertheless, a comprehensive performance analysis of LB communication systems is still lacking in the literature. In fact, none of the aforementioned work has considered the main features that characterize LB such as finite phases and the double fading channel.

In this paper, we comprehensively analyze LB modulation from various aspects, i.e., temporal, spectral, and error performance characteristics. More precisely, we provide the first expression for the LB modulated signal that accounts for the reduced complexity of the system compared to LoRa. The reason is that the number of antenna loads is finite, limiting the number of available phases for the signal.

Based on the provided signal expression, we analytically derive a closed-form expression for the power spectrum of baseband LB signals. The derivation of the power spectral density involves integration over the non-linear phase quantization function. The spectral analysis provides a better understanding of the adjacent channel interference for LB modulation and its relation to the number of loads (i.e., system complexity) [41].

Also, we derive the optimal decoder for LB, i.e., ML, and compare it with the conventional FFT decoder. For ML and FFT decoder, we conduct error performance analysis in AWGN and fading channels. More precisely, we derive closed-form approximations for the SER in both AWGN and double Nakagami-m fading channels for fixed transmit power. Besides, given a constraint on the average transmit power, we provide the optimal power allocation scheme using water-filling and analyze the corresponding average SER.

The performance analysis of LB is quite involving compared to normal LoRa. For instance, unlike normal LoRa, the LB waveforms representing different symbols are not orthogonal when sampled at the Nyquist rate. This leads to a SER expression involving a product of Marcum Q functions with different shape parameters. Additionally, the PDF of the cascaded Nakagami-m fading channel entails integration over a modified Bessel function of the second kind, putting further the difficulty in numerical evaluation.

The contribution of this paper can be summarized as follows:

- We provide a novel signal expression in the time-domain for LB signal with a generalized number of loads.
- We derive a closed-form expression for the power spectrum of LB signals and investigate whether LB meets the regulation of European Telecommunications Standards Institute (ETSI) for adjacent channel interference.
- We provide a ML-based decoder for LB.

TABLE I: Table of Symbols

Symbol	Meaning
$D$	decoder type
$\sigma^2$	noise power per dimension
$\gamma$	SNR
$E_s, \bar{E}_s$	instantaneous, average symbol energy
$a, i$	transmit symbol index, decoder output bin index
$\mathcal{L}_{(a,i)}^D$	$i$ -th decoder output bin value for symbol $a$
$\hat{\mathcal{L}}_{(a)}^D$	$\max_{i,i \neq a} \{ \mathcal{L}_{(a,i)}^D \}$
$\xi_{(a,i)}^D$	decoder outputs without noise
$\mathcal{W}_{(a,i)}^D$	noise at the decoder
$\mu_a, \sigma_a^2$	expectation and variance of $\mathcal{L}_{(a,a)}^D$
$d_1, d_2$	link distances of the Tx-tag and tag-Tx links
$m, \Omega$	shape and spread parameter of Nakagami distribution
$r, v, n$	$m/\Omega, m_1 + m_2$ , and $ m_1 - m_2 $
$x_t, \omega_t, N_{GH}$	points, weights, and number of points in GH quadrature
$x_e, \omega_e, N_{GL}$	points, weights, and number of points in GL quadrature

- We derive closed-form approximations for the SER of LB in both AWGN and double Nakagami-m fading channels, considering both FFT and ML decoders.
- We study the SER performance of LB for various power allocation schemes, i.e., fixed and optimized power allocation techniques.

### C. Notations

Throughout this paper, we denote the Tx-tag and tag-Rx links with subscripts 1 and 2, respectively, vectors with bold small letters, random variables (r.v.s) with calligraphic letters, e.g.,  $\mathcal{L}$ , the PDF of  $\mathcal{L}$  with  $f_{\mathcal{L}}(l)$ , the cumulative distribution function (CDF) of  $\mathcal{L}$  with  $F_{\mathcal{L}}(l)$ , the expectation and variance of  $\mathcal{L}$  with  $\mathbb{E}[\mathcal{L}]$  and  $\mathbb{V}[\mathcal{L}]$ , respectively, complex Gaussian distribution that has mean  $\mu$  and variance  $\sigma^2$  with  $\mathcal{CN}(\mu, \sigma^2)$ , complex conjugate of a complex variable  $x$  with  $x^*$ , and inner product of vectors  $\alpha$  and  $\beta$  with  $\langle \alpha, \beta \rangle$ . The main symbols considered in this paper are listed in Table I.

### D. Structure of the paper

The remainder of this paper is structured as follows. First, the system model is presented in Section II, and the spectral analysis of LB is provided in Section III. In Section IV, the error performance in AWGN and fading channels are investigated. Then, the numerical results are presented in Section V, and Section VI concludes this paper.

## II. SYSTEM SETUP AND SIGNAL MODEL

In this section, we first explain the system setup and channel model for LB communication systems. Then, we provide the analytical expressions for LB signals, and we propose two decoders for LB.

### A. System Setup and Channel Model

We consider a LB communication system with a Tx generating a carrier wave, a backscatter tag, and a Rx, as shown in Fig. 1. The Tx sends a single-tone excitation wave to the tag with carrier frequency  $f_c$ . Then, the tag modulates

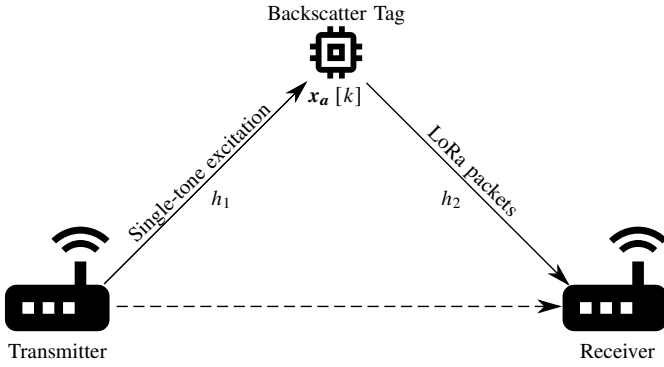


Fig. 1: Considered LB communication system.

the excitation signal with its data using CSS modulation and reflects it to the Rx. We consider a scheme where the tag introduces a frequency offset  $\Delta f$  to the incoming signal, shifting it to a channel centered at  $f_c + \Delta f$  to avoid interference from the direct link between Tx and Rx [15]. LB networks can be scaled by considering different SFs and/or carrier frequencies with negligible interference among users.

Also, we consider a flat double fading channel, where the complex channel gains of the Tx-tag and tag-Rx links are represented by  $h_1$  and  $h_2$ , respectively. The received signal, sampled at the Nyquist rate, can be expressed as

$$r_a[k] = h_1 h_2 \sqrt{E_s} x_a[k] + \omega[k], \forall k \in \{0, 1, \dots, M-1\}, \quad (1)$$

where  $E_s$  denotes the baseband symbol energy,  $x_a[k]$  denotes  $k^{\text{th}}$  sample of the baseband LB signal with data symbol  $a$ , and  $\omega[k]$  represents the thermal noise drawn from  $\mathcal{CN}(0, 2\sigma^2)$ . For simplicity, the multiplication of two channel gains can be expressed in an overall channel gain  $h$ , i.e.,  $h \triangleq h_1 h_2$ . This channel model includes the case of monostatic BC by considering  $h_1 = h_2 = \sqrt{h}$ .

In the following, we explain the backscatter process and provide analytical expressions for LB baseband signals.

### B. Backscatter Process and Signal Model

The reflected LoRa signals are synthesized by the RF switch that toggles between different antenna loads to create a set of reflection coefficients. The set of coefficients is selected to change the amplitude and phase of the incoming signal  $S_{\text{in}}$ . More precisely, let us define  $\Gamma_L$  and  $\Gamma_A$  as the load impedance and antenna impedance, respectively. The reflected signal  $S_{\text{out}}$  can be expressed as

$$S_{\text{out}}(t) = \frac{\Gamma_L(t) - \Gamma_A}{\Gamma_L(t) + \Gamma_A} S_{\text{in}}(t) = |\Gamma_T(t)| e^{j\theta_T(t)} S_{\text{in}}(t), \quad (2)$$

where the change of  $\Gamma_L(t)$  is discrete so that the possible number of phases  $\theta_T(t)$  and amplitudes  $|\Gamma_T(t)|$  are limited. However, to perfectly synthesize LoRa signals, we need an infinite number of phases so that the backscattered signals are only approximations of the ideal sinusoidal waves. For this reason, increasing the number of phases in LB can enhance the system performance and approach traditional LoRa systems.

<sup>1</sup> $\Delta f$  is typically 3 orders of magnitude lower than  $f_c$ .

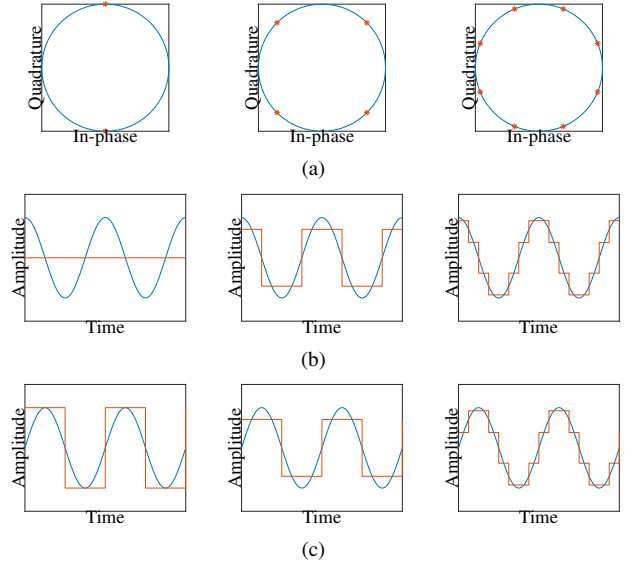


Fig. 2: IQ components comparison of backscattered waves (red) and sinusoidal waves (blue). The first, second, and third columns represent two, four, and eight phases, respectively: (a) phase diagram, (b) in-phase components, and (c) quadrature components.

On the other hand, increasing the number of possible phases raises not only the design complexity by adding more loads, but also the switching frequency, reducing the tag service life.

We first elaborate on some typical cases, i.e., using two, four, and eight phases to approximate sine and cosine. Then, we generalize the model. As shown in the first, second, and third columns in Fig. 2, we compare the IQ components of approximated sinusoidal waves (marked with red) with pure sinusoidal waves (marked with blue).

If we consider only two phases for LB, the in-phase component of the backscattered wave is zero while the quadrature component is a square wave. To avoid interference with the direct link, a frequency shift  $\Delta f$  should be introduced. In normal non-BC systems, the frequency shift is realized by multiplying the original signals centered at  $f_c$  by a sinusoid with frequency  $\Delta f$ . However, due to the limited number of loads in BC tags, it is introduced through multiplication with square waves with frequency  $\Delta f$ , resulting in additional harmonics [16]. More precisely, while moving the LoRa signals into the channel centered at  $f_c + \Delta f$ , a mirror copy centered at  $f_c - \Delta f$  is also created. Also, there are harmonics centered at  $f_c \pm 3\Delta f$ ,  $f_c \pm 5\Delta f$ ,  $f_c \pm 7\Delta f$ , etc.

If the system adopts four loads, both in-phase and quadrature components are square waves. This scheme cancels the mirror copies of the spectra. Nevertheless, the harmonics are preserved at  $f_c - 3\Delta f$ ,  $f_c + 5\Delta f$ ,  $f_c - 7\Delta f$ , etc [14]. When considering eight loads, two more voltage levels are added to the approximated sinusoids. The staircase-like waveforms cancels at least the harmonics centered at  $f_c - 3\Delta f$  and  $f_c + 5\Delta f$  [15]. Also, higher-order harmonics can be canceled by adding more phases if required.

In this regard, unlike conventional LoRa, LB has a finite

number of phases in addition to several harmonics. In the following, we provide the signal expressions for the baseband signals accounting for the finite phases.

1) *Continuous-Time Description*: The baseband LB signals are synthesized by switching between different loads so that they only have a limited number of phases, making them an approximation to the normal LoRa signals.

To generalize the model, let us consider the number of loads written in a form of  $2^N$ , where  $N \in \{1, 2, 3, \dots\}$ . The phases are evenly distributed and rotationally symmetric in the phase diagram at position  $(2n-1)\pi/2^N$ ,  $\forall n \in \{1, 2, \dots, 2^N\}$  with some examples shown in Fig. 2a.

We introduce to the phase of conventional LoRa signal a mid-rise quantizer to perfectly model the discrete phases of LB. The quantizer maps the infinite phases of the LoRa modulation into a finite set of phases in LB. More precisely, the mid-rise quantization function with  $2^N$  levels for input value  $x \in (-\pi, \pi)$  is given by

$$\tilde{Q}_N(x) = \frac{\lfloor 2^{N-1}x/\pi \rfloor + \frac{1}{2}}{2^{N-1}/\pi}, \quad (3)$$

where  $\lfloor \cdot \rfloor$  is the floor function [42]. Let us also specify the periodicity of the quantization function as  $\tilde{Q}_N(x+2\pi) \triangleq \tilde{Q}_N(x)$  for any real input value  $x$ , making it consistent with the periodic change of the phase.

Let  $T_s \triangleq M/B$  be the symbol duration, the instantaneous phase of LoRa modulation with symbol  $a$  for interval  $[0, T_s]$  can be given in [4] as

$$\hat{\phi}_a(t) = 2\pi Bt \left[ \frac{a}{M} - \frac{1}{2} + \frac{Bt}{2M} - u(t - \tau_a) \right], \quad (4)$$

where  $B$  denotes the bandwidth of LoRa,  $M = 2^{\text{SF}}$ ,  $\text{SF} \in \{7, 8, \dots, 12\}$  denotes the spreading factor, and  $\tau_a = (M-a)/B$  denotes the time instant of the sudden frequency change. Thus, the instantaneous phase of LB with symbol  $a$  is calculated as

$$\phi_a(t) = \tilde{Q}_N[\hat{\phi}_a(t)]. \quad (5)$$

Thus, the complex envelope for LB waveform of symbol  $a$  with unit power is calculated using (5) as

$$\begin{aligned} x_a(t) &= \exp\{j\phi_a(t)\} \\ &= \exp\left\{j\tilde{Q}_N\left[2\pi Bt\left[\frac{a}{M} - \frac{1}{2} + \frac{Bt}{2M} - u(t - \tau_a)\right]\right]\right\}. \end{aligned} \quad (6)$$

2) *Discrete-Time Description*: Let us consider the simple receiver implementation that sample the received signal at the chip rate, i.e.,  $1/T_c = M/T_s = B$ , the  $M$  samples in the interval  $[0, T_s]$ , for  $k \in \{0, 1, \dots, M-1\}$ , are

$$\begin{aligned} \phi_a(kT_c) &= \tilde{Q}_N\left[\frac{k\pi}{M}(2a - M + k) - 2M\pi u\left(\frac{k+a-M}{B}\right)\right] \\ &= \tilde{Q}_N\left[\frac{k\pi}{M}(2a - M + k)\right], \end{aligned} \quad (7)$$

where the last equality is due to the fact that  $2M\pi u(\cdot)$  is always an integer multiple of  $2\pi$  for all  $k$  and  $\tilde{Q}_N(x)$  is periodic of  $2\pi$ . Normalizing the total energy of the samples, we

have the discrete-time expression of the baseband LB signal with  $2^N$  quantization phases

$$x_a[k] = \sqrt{\frac{1}{M}} \exp\left\{j\tilde{Q}_N\left[\frac{k\pi}{M}(2a - M + k)\right]\right\}, \quad k \in \{0, 1, \dots, M-1\}. \quad (8)$$

### C. LoRa backscatter Decoders

We study the error performance of LB under two decoders, i.e., the ML and FFT decoders. We consider that the overall channel amplitude  $|h| = |h_1||h_2|$  is known to the Rx, and it performs non-coherent detection.<sup>2</sup>

1) *Maximum Likelihood Decoder*: The optimum detector in an AWGN channel is the ML detector if all the symbols are equiprobable [44]. The decoder performs cross-correlation on the received signal with all possible waveforms and chooses the symbol that has the largest absolute value of cross-correlation with the received signal, i.e.,

$$\hat{a} = \arg \max_{0 \leq i \leq M-1} |\langle \mathbf{r}_a, \mathbf{x}_i^* \rangle| \quad (9)$$

$$= \arg \max_{0 \leq i \leq M-1} \left| \sum_{k=0}^{M-1} r_a[k] \cdot x_i^*[k] \right|, \quad (10)$$

where  $\hat{a}$  is the symbol decision made by the Rx,  $x_i^*[k]$  is the complex conjugate of  $x_i[k]$ . The ML decoder is the optimum decoder for LB as shown in Appendix A. However, LB is a relatively high-order modulation that reaches  $M = 4096$  for  $\text{SF} = 12$ , resulting in a more complicated design and implementation of the decoder.

2) *FFT Decoder*: The process of FFT decoder follows three steps. First, The received signal is firstly multiplied by a complex down-chirp signal  $x_d[k]$

$$\tilde{r}_a[k] = r_a[k] x_d[k] = r_a[k] \sqrt{\frac{1}{M}} e^{-j2\pi\frac{k^2}{2M} + j\pi k}, \quad (11)$$

where the dechirped signal  $\tilde{r}_a[k]$  is called the twisted signal. The symbol decision is made by choosing the maximum value among  $M$ -bin discrete Fourier transform (DFT) output on  $\tilde{r}_a[k]$

$$\hat{a} = \arg \max_{0 \leq i \leq M-1} |\text{DFT}(\tilde{r}_a[k])| \quad (12)$$

$$= \arg \max_{0 \leq i \leq M-1} \left| \sum_{k=0}^{M-1} \tilde{r}_a[k] e^{-j2\pi ki/M} \right|. \quad (13)$$

It has been proven that the two decoders are equivalent for normal LoRa [4] but this is not valid for LB. Also, the waveforms representing different symbols sampled at the chip rate  $B$  are non-orthogonal. Fig. 3 compares the cross-correlation of LB waveforms (4 quantization phases) with that of normal LoRa at  $\text{SF} = 7$ . It shows that the cross-correlation of LB waveforms has numerous non-zero values while the cross-correlation between different symbols are all zero for

<sup>2</sup>Non-coherent detectors for LB can provide a good trade-off between the performance and complexity since the performance improvement using coherent detectors is only 0.7 dB for traditional LoRa [43].

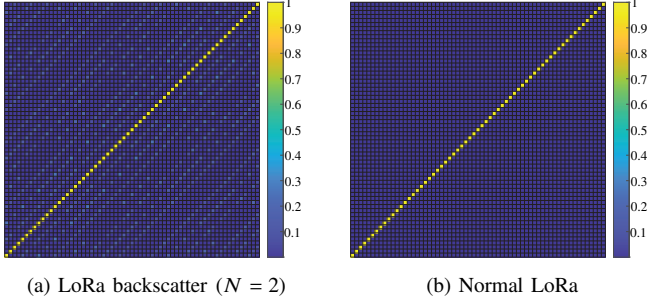


Fig. 3: The cross-correlation of LB and LoRa symbols when SF = 7.

TABLE II: Maximum cross-correlation value between different LB waveforms for  $N \in \{2, 3, 4, 5\}$  and SF  $\in \{7, 8, \dots, 12\}$ .

	SF=7	SF=8	SF=9	SF=10	SF=11	SF=12
N=2	0.250	0.156	0.156	0.117	0.086	0.067
N=3	0.125	0.082	0.107	0.064	0.071	0.050
N=4	0.000	0.000	0.053	0.032	0.043	0.024
N=5	0.000	0.000	0.000	0.000	0.022	0.013

normal LoRa<sup>3</sup>. However, most of the non-zero correlation values are relatively small, indicating that the symbols are not strongly correlated.

In Table. II, we show the maximum cross-correlation value between different LB waveforms for  $N \in \{2, 3, 4, 5\}$  and SF  $\in \{7, 8, \dots, 12\}$ . The cross-correlation generally decreases as  $N$  and SF increase.

### III. SPECTRAL ANALYSIS

The power spectrum of the LB modulation is analytically determined in closed form in this section. We consider a source that produces a random symbol sequence where all the symbols are independent, identically distributed with random variables  $\mathcal{B}_n$ . Assuming that the symbols are equiprobable, we have

$$P(\mathcal{B}_n = a) = \frac{1}{M}, \quad a \in \{0, 1, \dots, M-1\}. \quad (14)$$

The time sequence of the LB waveforms can be expressed with a random process

$$I(t) = \sum_n x_s(t - nT_s; \mathcal{B}_n) g_{T_s}(t - nT_s), \quad (15)$$

where  $g_{T_s}$  is a rectangular function with width  $T_s$ . The power spectrum density of the random process  $I(t)$  can be derived as

$$\mathcal{G}_I(f) = \mathcal{G}_I^{(c)}(f) + \mathcal{G}_I^{(d)}(f). \quad (16)$$

where  $\mathcal{G}_I^{(c)}(f)$  and  $\mathcal{G}_I^{(d)}(f)$  are the continuous and a discrete parts of the spectrum, respectively. The continuous and discrete spectrum in (16) can be obtained by applying frequency

<sup>3</sup>LoRa symbols are non-orthogonal, it can be proven orthogonal only when sampled at Nyquist rate.

domain analysis of randomly modulated signals for the random process [45]

$$\mathcal{G}_I^{(c)}(f) = \frac{1}{T_s} \left[ \sum_{a=0}^{M-1} \frac{1}{M} |S_a(f)|^2 - \left| \sum_{a=0}^{M-1} \frac{1}{M} S_a(f) \right|^2 \right], \quad (17)$$

$$\mathcal{G}_I^{(d)}(f) = \frac{1}{M^2 T_s^2} \sum_{l=-\infty}^{\infty} \left| \sum_{a=0}^{M-1} S_a\left(\frac{lB}{M}\right) \right|^2 \delta\left(f - \frac{lB}{M}\right), \quad (18)$$

where  $\{S_a(f)\}_{a=0}^{M-1}$  are the Fourier transforms of the waveforms  $\{x_a(t)\}_{a=0}^{M-1}$  from the modulator.

The Fourier transform of the complex envelope can be expressed as

$$\begin{aligned} S_a(f) &= \int_0^{T_s} e^{j\tilde{Q}_N[2\pi Bt[\frac{a}{M} - \frac{1}{2} + \frac{Bt}{2M} - u(t - \frac{M-a}{B})]]} e^{-j2\pi f t} dt \\ &= \int_0^{\frac{M-a}{B}} e^{j\tilde{Q}_N[2\pi Bt(\frac{a}{M} - \frac{1}{2} + \frac{Bt}{2M})]} e^{-j2\pi f t} dt + \\ &\quad \int_{\frac{M-a}{B}}^{\frac{B}{M}} e^{j\tilde{Q}_N[2\pi Bt(\frac{a}{M} - \frac{3}{2} + \frac{Bt}{2M})]} e^{-j2\pi f t} dt. \end{aligned} \quad (19)$$

Leveraging the periodicity of  $\tilde{Q}_N(\cdot)$ , we rewrite the second term in (19) as

$$\int_{\frac{M-a}{B}}^{\frac{B}{M}} e^{j\pi\tilde{Q}_N[2\pi Bt(\frac{a}{M} - \frac{3}{2} + \frac{Bt}{2M}) + 2\pi(M-a)]} e^{-j2\pi f t} dt. \quad (20)$$

Let us also define  $f_1(t) \triangleq 2\pi Bt(\frac{a}{M} - \frac{1}{2} + \frac{Bt}{2M})$ , and  $f_2(t) \triangleq 2\pi Bt(\frac{a}{M} - \frac{3}{2} + \frac{Bt}{2M}) + 2\pi(M-a)$  as the two terms within  $\tilde{Q}_N(\cdot)$  of two integral parts. Let us define  $f(t)$  as

$$f(t) \triangleq \begin{cases} f_1(t) & , \quad 0 \leq t < \frac{M-a}{B} \\ f_2(t) & , \quad \frac{M-a}{B} \leq t \leq \frac{B}{M} \end{cases}$$

It is worth noting that,  $f(t)$  is a continuous function with  $f_1(\frac{M-a}{B}) = f_2(\frac{M-a}{B})$ . Thus, the sum of two separated integrals in (19) can be replaced with one integral

$$S_a(f) = \int_0^{\frac{B}{M}} e^{j\tilde{Q}_N[f(t)]} e^{-j2\pi f t} dt. \quad (21)$$

It is challenging to directly compute the integral in (21) with the quantization function inside. However, one possible solution is to divide the integral interval into slots, as shown in Fig. 4. The value of  $\tilde{Q}_N[f(t)]$  remains unchanged in each intervals divided by a time set  $\{t_m\}_{m=1}^{\psi}$ . Details about obtaining  $\{t_m\}_{m=1}^{\psi}$  are provided in Appendix B. The integral in each slot can be calculated as

$$\begin{aligned} I_m(f) &= \int_{t_m}^{t_{m+1}} e^{j\tilde{Q}_N[f(t)]} e^{-j2\pi f t} dt \\ &= \frac{j}{2f} e^{j\pi\tilde{Q}_N[f(\frac{t_m+t_{m+1}}{2})]} \left( e^{-j2\pi f t_{m+1}} - e^{-j2\pi f t_m} \right), \end{aligned} \quad (22)$$

where  $(t_m + t_{m+1})/2$  can be replaced by any real value between  $t_m$  and  $t_{m+1}$ .

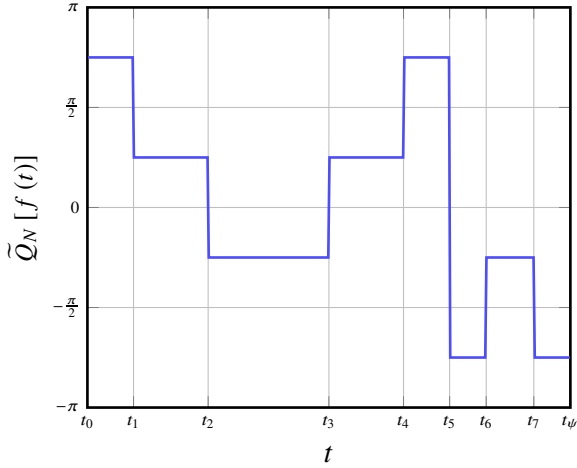


Fig. 4: An example of  $\tilde{Q}_N[f(t)]$  as a function of time at  $N = 2$ .

Since we have  $f(0) = f(M/B) = 0$ , the overall integral interval begins with  $t_0$  and ends with  $t_\psi$ . Thus, the integral in (19) is calculated as a sum of  $I_m(f)$

$$S_a(f) = \frac{j}{2\pi f} \sum_{m=1}^{\psi-1} e^{j\pi \tilde{Q}_N[f(\frac{t_m+t_{m+1}}{2})]} \left( e^{-j2\pi f t_{m+1}} - e^{-j2\pi f t_m} \right). \quad (23)$$

By substituting (23) into (17) and (18), we can calculate both the continuous and discrete parts of the spectrum for baseband LB signals.

#### IV. PERFORMANCE ANALYSIS

In this section, we derive the SER of the LB communication system in terms of different decoders, channel models, and power strategies.

##### A. LoRa backscatter SER Performance over AWGN Channels

The SER in an AWGN channel is a conditional probability conditioned on the overall channel gain  $h$ . Thus, we consider  $h$  as a constant in this subsection. We define the r.v.  $\mathcal{L}_{(a,i)}^D$  as the absolute value of  $i$ -th bin of  $D \in \mathbb{D} \triangleq \{\text{ML}, \text{FFT}\}$  decoder when symbol  $a$  is transmitted. For ML decoder,  $\mathcal{L}_{(a,i)}^{\text{ML}}$  is calculated as

$$\mathcal{L}_{(a,i)}^{\text{ML}} = \left| \sum_{k=0}^{M-1} r_a[k] x_i^*[k] \right| \quad (24)$$

$$= \left| h\sqrt{E_s} \xi_{(a,i)}^{\text{ML}} + \mathcal{W}_{(a,i)}^{\text{ML}} \right|, \quad (25)$$

where  $\xi_{(a,i)}^{\text{ML}} = \sum_{k=0}^{M-1} x_a[k] x_i^*[k]$  is the cross-correlation between the transmitted waveform and the  $i$ -th reference signal and  $\mathcal{W}_{(a,i)}^{\text{ML}} = \sum_{k=0}^{M-1} \omega[k] x_i^*[k]$  is the noise projection of the reference signals, following complex Gaussian distribution with variance  $2\sigma^2$ . For FFT decoder,  $\mathcal{L}_{(a,i)}^{\text{FFT}}$  is

$$\mathcal{L}_{(a,i)}^{\text{FFT}} = |\text{DFT}(r_a[k] x_d[k])| \quad (26)$$

$$= \left| h\sqrt{E_s} \xi_{(a,i)}^{\text{FFT}} + \mathcal{W}_{(a,i)}^{\text{FFT}} \right|, \quad (27)$$

where  $\xi_{(a,i)}^{\text{FFT}} = \text{DFT}(x_a[k] x_d[k])$  denotes the  $i$ -th bin of the DFT for the dechirped reference signals and  $\mathcal{W}_{(a,i)}^{\text{FFT}} = \text{DFT}(\omega[k] x_d[k])$  is the  $i$ -th bin of the DFT for the dechirped complex white Gaussian noise, which also follows complex Gaussian distribution with variance  $2\sigma^2$ . Since (25) and (27) have the same pattern, i.e., the absolute value of a sum of a complex constant and a complex Gaussian r.v.,

$$\mathcal{L}_{(a,i)}^D = \left| h\sqrt{E_s} \xi_{(a,i)}^D + \mathcal{W}_{(a,i)}^D \right|, \quad (28)$$

which follows Rician distribution with shape parameter  $\kappa_{(a,i)}^D = \left| h\sqrt{E_s} \xi_{(a,i)}^D \right|^2 / 2\sigma^2$ , as shown in Appendix C. Without losing generality, if  $\xi_{(a,i)}^D = 0$ , the shape parameter is zero so that the Rician distribution becomes Rayleigh distribution.

It is worth noting that the r.v.s in the set  $\left\{ \mathcal{L}_{(a,i)}^{\text{ML}} \right\}_{i=0}^{M-1}$  are not independent because  $\mathcal{W}_{(a,i)}^{\text{ML}}$  are the noise projection of non-orthogonal waveforms, as shown in Fig. 3a. On the other hand, the r.v.s in the set  $\left\{ \mathcal{L}_{(a,i)}^{\text{FFT}} \right\}$  are independent since the noise is projected to the directions of orthogonal basis in the DFT process. The dependence of  $\left\{ \mathcal{L}_{(a,i)}^{\text{ML}} \right\}_{i=0}^{M-1}$  make it challenging to find their joint distribution. However, they are approximately independent for the following three reasons. First, as shown in Fig. 3a, most of the cross-correlation values are zero, namely, most of the r.v.s within  $\left\{ \mathcal{L}_{(a,i)}^{\text{ML}} \right\}_{i=0}^{M-1}$  are independent. Second, the non-zero cross-correlation values are relatively small so that the dependent r.v.s are not strongly correlated. Also, the non-zero cross-correlation values decrease as the number of quantization phases or the spreading factor increases. Nevertheless, ignoring the correlation makes the derived expression an upper bound to the exact SER [44, Section 4.5-4]. In the following, we assuming that  $\left\{ \mathcal{L}_{(a,i)}^{\text{ML}} \right\}_{i=0}^{M-1}$  are independent so that the derivation applies to both decoders.

To obtain an expression for the SER, let us define the instantaneous SNR as

$$\gamma = \frac{|h|^2 E_s / T_s}{2\sigma^2 B} = \frac{|h|^2 E_s}{2\sigma^2 M}. \quad (29)$$

The PDF and CDF of  $\mathcal{L}_{(a,i)}^D$  conditioned on the overall channel gain  $h$  can be written for  $D \in \mathbb{D}$  as

$$f_{\mathcal{L}_{(a,i)}^D|h}(l) = \frac{l}{\sigma^2} \exp\left[-\frac{(l^2 + C^2)}{2\sigma^2}\right] I_0\left(\frac{lC}{\sigma^2}\right), \quad (30)$$

$$F_{\mathcal{L}_{(a,i)}^D|h}(l) = 1 - Q_1\left(\frac{C}{\sigma}, \frac{l}{\sigma}\right), \quad (31)$$

where  $C = \left| h\sqrt{E_s} \xi_{(a,i)}^D \right|$ ,  $Q_1(\cdot)$  is the Marcum Q-function of order one [46, eq: 7],  $I_0(\cdot)$  is the modified Bessel function of the first kind and order zero [47, eq: 9.6.1].

The detection error happens when  $\hat{a} \neq a$ , i.e.,  $\mathcal{L}_{(a,a)}^D$  is not maximum among the set  $\left\{ \mathcal{L}_{(a,i)}^D \right\}_{i=0}^{M-1}$ . In other words, the symbol error probability (SEP) can be calculated by comparing the correct bin, namely,  $\mathcal{L}_{(a,a)}^D$ , with the maximum of the noisy

TABLE III: Typical values of  $\kappa_{(a,a)}^D$ ,  $\mu_a$ , and  $\sigma_a^2$  for  $N \in \{2, 3, 4, 5\}$  at SF = 7,  $\gamma = -10$  dB, and  $a = h = E_s = 1$ .

N	$\kappa_{(a,a)}^D$		$\mu_a$		$\sigma_a^2$	
	ML	FFT	ML	FFT	ML	FFT
2	12.80	10.51	26.11	23.75	25.08	24.96
3	12.80	12.27	26.11	25.58	25.08	25.05
4	12.80	12.71	26.11	26.01	25.08	25.07
5	12.80	12.78	26.11	26.09	25.08	25.08

bins. Thus, we define  $\hat{\mathcal{L}}_{(a)}^D \triangleq \max_{i, i \neq a} \{\mathcal{L}_{(a,i)}^D\}$  whose CDF of  $\hat{\mathcal{L}}_{(a)}^D$  can be computed using order statistics as

$$\begin{aligned} F_{\hat{\mathcal{L}}_{(a)}^D | h}(l) &= \prod_{i=0, i \neq a}^{M-1} F_{\mathcal{L}_{(a,i)}^D | h}(l) \\ &= \prod_{i=0, i \neq a}^{M-1} \left[ 1 - Q_1 \left( \frac{|h\sqrt{E_s}\xi_{(a,i)}^D|}{\sigma}, \frac{l}{\sigma} \right) \right]. \end{aligned} \quad (32)$$

The conditional SEP using  $D \in \mathbb{D}$  decoder given a transmit symbol  $a$  is calculated as

$$\begin{aligned} P_{e|a}^D &= P \left( \hat{\mathcal{L}}_{(a)}^D > \mathcal{L}_{(a,a)}^D | h \right) \\ &= \int_0^\infty \left[ 1 - F_{\hat{\mathcal{L}}_{(a)}^D | h}(l) \right] f_{\mathcal{L}_{(a,a)}^D | h}(l) dl, \end{aligned} \quad (33)$$

where the shape parameter of  $\mathcal{L}_{(a,a)}^D$  is

$$\kappa_{(a,a)}^D = \left| h\sqrt{E_s}\xi_{(a,a)}^D \right|^2 / 2\sigma^2 \quad (34)$$

$$= \left| \xi_{(a,a)}^D \right|^2 M \gamma. \quad (35)$$

The Rician distributed r.v.  $\mathcal{L}_{(a,a)}^D$  can be approximated as a Gaussian r.v. if the shape parameter  $\kappa_{(a,a)}^D$  is larger than 2 [48]. In our setting, as shown in (35),  $\xi_{(a,a)}^D \approx 1$  and  $M = 2^{\text{SF}}$  ranging from  $2^7 = 128$  to  $2^{12} = 4096$  is a large number so that  $\mathcal{L}_{(a,a)}^D$  can be approximated as a Gaussian r.v. in an acceptable SNR range. For example, if we consider SF = 8 and ML decoder, we have  $\xi_{(a,a)}^{\text{ML}} = 1$  and  $M = 256$ . The proper SNR range for the approximation is  $\gamma \geq 1/128 \approx -21.1$  dB, which covers most of the SER range of interest. Hence, we have

$$f_{\mathcal{L}_{(a,a)}^D | h}(l) \approx \frac{1}{\sqrt{2\pi\sigma_a^2}} \exp \left[ -\frac{(l - \mu_a)^2}{2\sigma_a^2} \right], \quad (36)$$

where  $\mu_a$  and  $\sigma_a$  are the mean and variance of  $\mathcal{L}_{(a,a)}^D$ , respectively, i.e.,

$$\mu_a = \mathbb{E} \left[ \mathcal{L}_{(a,a)}^D \right] = \sigma \sqrt{\pi/2} \cdot L_{1/2} \left( -\kappa_{(a,a)}^D \right), \quad (37)$$

$$\sigma_a^2 = \mathbb{V} \left[ \mathcal{L}_{(a,a)}^D \right] = 2\sigma^2 \left( 1 + \kappa_{(a,a)}^D \right) - \mu_a^2, \quad (38)$$

where  $L_q(\cdot)$  denotes a Laguerre polynomial [47, eq: 13.6.27], and for the case  $q = 1/2$ , we have

$$L_{1/2}(x) = e^{x/2} \left[ (1-x) I_0 \left( -\frac{x}{2} \right) - x I_1 \left( -\frac{x}{2} \right) \right]. \quad (39)$$

In Table. III, we show some typical values of  $\kappa_{(a,a)}^D$ ,  $\mu_a$ , and  $\sigma_a^2$  as a function of  $N$  for both ML and FFT decoders.

The complexity of evaluating integral (33) mainly comes from the product of  $M - 1$  non-identical Rician CDFs. As a possible solution, we can leverage an asymptotic approximation of the order statistics of a sequence of independent and non-identically distributed (i.n.i.d.) Rician r.v.s [49] using the extreme value theorem (EVT). Nevertheless, it shall result in an exponential-in-exponential expression, rendering difficulties in the integration.

Alternatively, we consider Gauss-Hermite quadrature to evaluate the integral numerically. In this procedure, the integral is converted to a weighted sum of function values using the Gauss-Hermite quadrature [47]. Since the Rician PDF (30) is zero for  $l < 0$ , the lower limit of integral (33) can be substituted with  $-\infty$ . Thus, we get

$$P_{e|a}^D \approx \int_{-\infty}^{\infty} \frac{\left[ 1 - F_{\hat{\mathcal{L}}_{(a)}^D | h}(l) \right]}{\sqrt{2\pi\sigma_a^2}} \exp \left[ -\frac{(l - \mu_a)^2}{2\sigma_a^2} \right] dl. \quad (40)$$

Let us define  $\hat{l} \triangleq (l - \mu_a) \sqrt{2}\sigma_a$  and substitute  $l$  with  $\sqrt{2}\sigma_a \hat{l} + \mu_a$  so that the integral becomes

$$P_{e|a}^D \approx \int_{-\infty}^{\infty} \left[ 1 - F_{\hat{\mathcal{L}}_{(a)}^D | h} \left( \sqrt{2}\sigma_a \hat{l} + \mu_a \right) \right] \frac{\exp \left[ -\hat{l}^2 \right]}{\sqrt{\pi}} d\hat{l} \quad (41)$$

$$\approx \frac{1}{\sqrt{\pi}} \sum_{t=1}^{N_{\text{GH}}} \omega_t \left[ 1 - F_{\hat{\mathcal{L}}_{(a)}^D | h} \left( \sqrt{2}\sigma_a x_t + \mu_a \right) \right], \quad (42)$$

where  $N_{\text{GH}}$  is the number of function samples used to approximate the integral,  $x_t$  are the roots of the physicists' version of the Hermite polynomial  $H_{N_{\text{GH}}}(x)$ , and  $\omega_t$  are the corresponding weights. The integration formula and corresponding weights can be found in [47, eq: 25.4.46].

We assume that the transmit symbols are equiprobable so that the average SER of LB in the AWGN channel can be expressed as

$$\begin{aligned} \overline{P_{e|h}^D} &= \frac{1}{M} \sum_{a=0}^{M-1} P_{e|a}^D \\ &= \frac{1}{M\sqrt{\pi}} \sum_{a=0}^{M-1} \sum_{t=1}^{N_{\text{GH}}} \omega_t \left[ 1 - F_{\hat{\mathcal{L}}_{(a)}^D | h} \left( \sqrt{2}\sigma_a x_t + \mu_a \right) \right]. \end{aligned} \quad (43)$$

### B. LoRa backscatter SER Performance over Double Nakagami-m Fading Channels

We consider a double Nakagami-m fading scenario with different shape parameters  $\{m_1, m_2\}$  and spread parameters  $\{\Omega_1, \Omega_2\}$ . The spread parameters are related to the link distance, i.e.,  $\Omega_1 \propto 1/d_1^2$  and  $\Omega_2 \propto 1/d_2^2$ , where  $\{d_1, d_2\}$  are the distances of the two links. Let us define r.v.s  $|\mathcal{H}_1|$  and  $|\mathcal{H}_2|$  as the channel amplitudes of Tx-tag and tag-Rx links, respectively. The PDFs of  $|\mathcal{H}_1|$  and  $|\mathcal{H}_2|$  can be expressed as

$$f_{|\mathcal{H}_1|}(|h_1|) = \frac{2m_1^{m_1}}{\Gamma(m_1)\Omega_1^{m_1}} |h_1|^{2m_1-1} \exp \left[ -\frac{m_1}{\Omega_1} |h_1|^2 \right], \quad (44)$$

$$f_{|\mathcal{H}_2|}(|h_2|) = \frac{2m_2^{m_2}}{\Gamma(m_2)\Omega_2^{m_2}} |h_2|^{2m_2-1} \exp \left[ -\frac{m_2}{\Omega_2} |h_2|^2 \right]. \quad (45)$$



Let us also define the r.v.  $|\mathcal{H}| \triangleq |\mathcal{H}_1| |\mathcal{H}_2|$  as the overall channel amplitude, whose PDF is governed by [50]

$$f_{|\mathcal{H}|}(|h|) = \frac{4(r_1 r_2)^{v/2}}{\Gamma(m_1)\Gamma(m_2)} |h|^{v-1} K_n(2\sqrt{r_1 r_2} |h|), \quad (46)$$

where  $\Gamma(\cdot)$  denotes the Gamma function [47, eq: 6.1.1],  $K_n(\cdot)$  denotes the modified Bessel function of the second kind with order  $n$  [47, eq: 9.6.1],  $r_1 = m_1/\Omega_1$ ,  $r_2 = m_2/\Omega_2$ ,  $v = m_1 + m_2$ , and  $n = |m_1 - m_2|$ .

In the following, we analyze two cases with different power allocation schemes, i.e., fixed transmit power and varying transmit power with an average power constraint.

1) *Fixed Transmit Power*: Considering the fixed symbol energy, the average SER in fading channels is calculated as

$$\overline{P_e^D} = \int_0^\infty \overline{P_{e|h}^D} f_{|\mathcal{H}|}(|h|) d|h|. \quad (47)$$

Substituting (43) and (46) into (47), and substituting  $|h|$  with  $\tilde{h}/2\sqrt{r_1 r_2}$ , we obtain

$$\overline{P_e^D} = \frac{2^{2-v}\sqrt{1/\pi}}{M\Gamma(m_1)\Gamma(m_2)} \sum_{a=0}^{M-1} \sum_{t=1}^{N_{GH}} \omega_t I_1, \quad (48)$$

where

$$I_1 = \int_0^\infty \left[ 1 - F_{\hat{\mathcal{L}}_{(a)}^D}(\tilde{h}) \left( \sqrt{2}\sigma_a x_t + \mu_a \right) \right] \tilde{h}^{v-1} K_n(\tilde{h}) d\tilde{h}. \quad (49)$$

In the following, we compute  $I_1$  depending on the value of  $n$  since for certain cases the Bessel function in (49) can be expressed in closed-form while for other cases it is challenging to find a closed-form expression.

a)  *$n$  is half-integer*: We consider the order of the Bessel function as a half-integer, i.e.,  $n = u + \frac{1}{2}$  for all  $u \in \{0, 1, 2, \dots\}$ . Thus, the modified Bessel function of the second kind with order  $n$  can be expressed in closed form [51, eq: 8.468]

$$K_{u+\frac{1}{2}}(z) = \sqrt{\frac{\pi}{2z}} \sum_{k=0}^u \frac{(u+k)!}{k!(u-k)!(2z)^k} e^{-z}. \quad (50)$$

Substituting (50) into  $I_1$  yields

$$I_1 = \int_0^\infty \sqrt{\frac{\pi}{2\tilde{h}}} \left[ 1 - F_{\hat{\mathcal{L}}_{(a)}^D}(\tilde{h}) \left( \sqrt{2}\sigma_a x_t + \mu_a \right) \right] \times \sum_{k=0}^{\lfloor n \rfloor} \frac{(\lfloor n \rfloor + k)!}{k!(\lfloor n \rfloor - k)!(2\tilde{h})^k} \tilde{h}^{v-1} e^{-\tilde{h}} d\tilde{h}. \quad (51)$$

where an a power and an exponential terms  $\tilde{h}^{v-1} e^{-\tilde{h}}$  are included in the integrand. Thus, unlike using Gauss-Hermite quadrature in (42) that integrates on an integrand with an exponential term  $e^{-\tilde{t}^2}$ , we consider Gauss-Laguerre quadrature to evaluate the integral numerically

$$I_1 \approx \sqrt{\frac{\pi}{2}} \sum_{e=1}^{N_{GL}} \omega_e \frac{G_t(x_e)}{\sqrt{x_e}} \sum_{k=0}^{\lfloor n \rfloor} \frac{(\lfloor n \rfloor + k)!}{k!(\lfloor n \rfloor - k)!(2x_e)^k}, \quad (52)$$

where  $G_t(x_e)$  is given by

$$G_t(x_e) = 1 - \prod_{i=0, i \neq a}^{M-1} \left[ 1 - Q_1 \left( \frac{x_e \sqrt{E_s} \xi_{(a,i)}^D}{2\sqrt{r_1 r_2} \sigma}, \frac{\sqrt{2}\sigma_a x_t + \mu_a}{\sigma} \right) \right],$$

$N_{GL}$  is the number of function samples,  $x_e$  are the roots of the generalized Laguerre polynomial  $L_{N_{GL}}^{(v-1)}(x)$ , and  $\omega_e$  are the corresponding weights [52].

Substituting (52) into (48), we obtain the average SER in double Nakagami- $m$  fading channel for the half-integer order  $n$

$$\overline{P_e^D} = \frac{2^{2/3-v}}{M\Gamma(m_1)\Gamma(m_2)} \sum_{a=0}^{M-1} \sum_{t=1}^{N_{GH}} \sum_{e=1}^{N_{GL}} \omega_t \omega_e \frac{G_t(x_e)}{\sqrt{x_e}} \times \sum_{k=0}^{\lfloor n \rfloor} \frac{(\lfloor n \rfloor + k)!}{k!(\lfloor n \rfloor - k)!(2x_e)^k}. \quad (53)$$

b)  *$n$  is not half-integer*: If  $n$  is not half-integer, it is challenging to obtain a closed-form expression for the modified Bessel function of the second kind with an order  $n$ . Thus, we provide an approximation for the Bessel function using the two Bessel functions with adjacent half-integer orders. The approximation is tight according to numerical results. We also assume that  $n$ , namely, the difference between the shape parameters of two channels, is larger than  $1/2$ . This is because the tag is typically placed closer to the Tx to send signals to a Rx farther away. The link with a shorter distance, i.e., the Tx-tag link, is more likely to have a Line-of-Sight (LOS) path, while the tag-Rx link is more likely to experience a more severe multipath fading effect.

For all  $n > 1/2$ , there exists only one integer  $u$  satisfying the condition

$$u - \frac{1}{2} < n < u + \frac{1}{2}. \quad (54)$$

Both  $K_{u-1/2}(x)$  and  $K_{u+1/2}(x)$  can be written in form of elementary functions with an exponential term, as shown in (50). Let us define a closed-form function  $K_{u,n}(x)$  as

$$K_{u,n}(x) = \left[ \frac{K_{u-1/2}(x)}{K_{u+1/2}(x)} \right]^{u-n} \sqrt{K_{u-1/2}(x) K_{u+1/2}(x)}, \quad (55)$$

The approximation is provided in [53] as

$$K_n(x) \approx C_{u,n} K_{u,n}(x), \quad (56)$$

where  $C_{u,n}$  is a constant given by

$$C_{u,n} = \frac{(u-1/2)^{u-n+1/2} \Gamma(n)}{\Gamma(u+1/2)} < 1. \quad (57)$$

Let us also define the summation term in  $K_{u-1/2}(x)$  and  $K_{u+1/2}(x)$  as

$$\Psi_{u-1/2}(x) = \sum_{k=0}^{u-1} \frac{(u-1+k)!}{k!(u-1-k)!(2x)^k}, \quad (58)$$

$$\Psi_{u+1/2}(x) = \sum_{k=0}^u \frac{(u+k)!}{k!(u-k)!(2x)^k}, \quad (59)$$

and  $\Psi_{u,n}(x)$  as

$$\Psi_{u,n}(x) = \left[ \frac{\Psi_{u-1/2}(x)}{\Psi_{u+1/2}(x)} \right]^{u-n} \sqrt{\Psi_{u+1/2}(x) \Psi_{u-1/2}(x)}. \quad (60)$$

Substituting (60) into (56) results in

$$K_n(x) \approx \sqrt{\frac{\pi}{2x}} C_{u,n} \Psi_{u,n}(x) e^{-x}, \quad (61)$$

which has an exponential term so that the generalized Gauss-Laguerre quadrature can be applied to compute  $I_1$ . Following similar steps, the approximation for the average SER under double Nakagami- $m$  fading channels is calculated as

$$\overline{P_e^D} = \frac{2^{2/3-v} C_{u,n}}{M\Gamma(m_1)\Gamma(m_2)} \sum_{a=0}^{M-1} \sum_{r=1}^{N_{GH}} \sum_{e=1}^{N_{GL}} \frac{\omega_r \omega_e G_t(x_e)}{\sqrt{x_e} \Psi_{u,n}(x_e)}, \quad (62)$$

2) *Limited Average Power*: We consider a scenario where the transmit power is under certain constraints. Also, the symbol energy  $E_s(\gamma)$  can be adjusted according to the channel condition, or similarly, instantaneous SNR. Let us define the instantaneous SNR as

$$\gamma = \frac{\overline{E_s} |h|^2}{2\sigma^2 M} = \tilde{\gamma} |h|^2, \quad (63)$$

where  $\overline{E_s}$  denotes the average symbol energy and  $\tilde{\gamma} \triangleq \overline{E_s}/2\sigma^2 M$ . The energy constraint is governed by

$$\int_0^\infty E_s(\gamma) f_\Gamma(\gamma) d\gamma \leq \overline{E_s}, \quad (64)$$

where  $f_\Gamma(\gamma)$  is the PDF of the instantaneous SNR.<sup>4</sup> It is determined only by the channel power gain  $|h|^2$ . Thus, we have

$$p_\Gamma(\gamma) = \frac{2(r_1 r_2 / \tilde{\gamma})^{v/2}}{\Gamma(m_1)\Gamma(m_2)} \gamma^{v/2-1} K_n\left(2\sqrt{r_1 r_2 \gamma / \tilde{\gamma}}\right). \quad (65)$$

We adopt water-filling scheme, the optimal power allocation scheme, to adjust the transmit power [54]. The scheme is governed by

$$\frac{E_s(\gamma)}{\overline{E_s}} = \begin{cases} \frac{1}{\gamma_0} - \frac{1}{\gamma}, & \gamma > \gamma_0 \\ 0, & \gamma \leq \gamma_0 \end{cases} \quad (66)$$

where the outage SNR  $\gamma_0$  is found by numerically solving

$$\int_{\gamma_0}^\infty \left(\frac{1}{\gamma_0} - \frac{1}{\gamma}\right) p(\gamma) d\gamma = 1. \quad (67)$$

Substituting (66) into (1) yields the expression of the received signal with power allocation

$$r_a[k] = \sqrt{\frac{\overline{E_s} |h|^2}{\gamma_0} - 2\sigma^2 M} x_a[k] + \omega[k]. \quad (68)$$

Following similar derivation, the average SER in double fading channels with water-filling scheme is calculated as

$$\overline{P_e^D} = \frac{1}{\int_{h_0}^\infty f_{|\mathcal{H}|}(|h|) d|h|} \int_{h_0}^\infty \int_0^\infty \left[1 - F_{\mathcal{L}^D(a)}(l)\right] \times f_{\mathcal{L}^D(a)|h}(l) f_{|\mathcal{H}|}(|h|) dl d|h|, \quad (69)$$

where  $h_0$  is the amplitude of the outage channel amplitude defined as  $h_0 = \sqrt{\gamma_0/\tilde{\gamma}}$ . The integral is divided by  $\int_{h_0}^\infty f_{|\mathcal{H}|}(|h|) d|h|$  since it is a conditional probability that the SNR is higher than the outage.

<sup>4</sup>Note that the randomness in the SNR permits analyzing energy harvesting schemes where the harvested energy can be considered as a r.v..

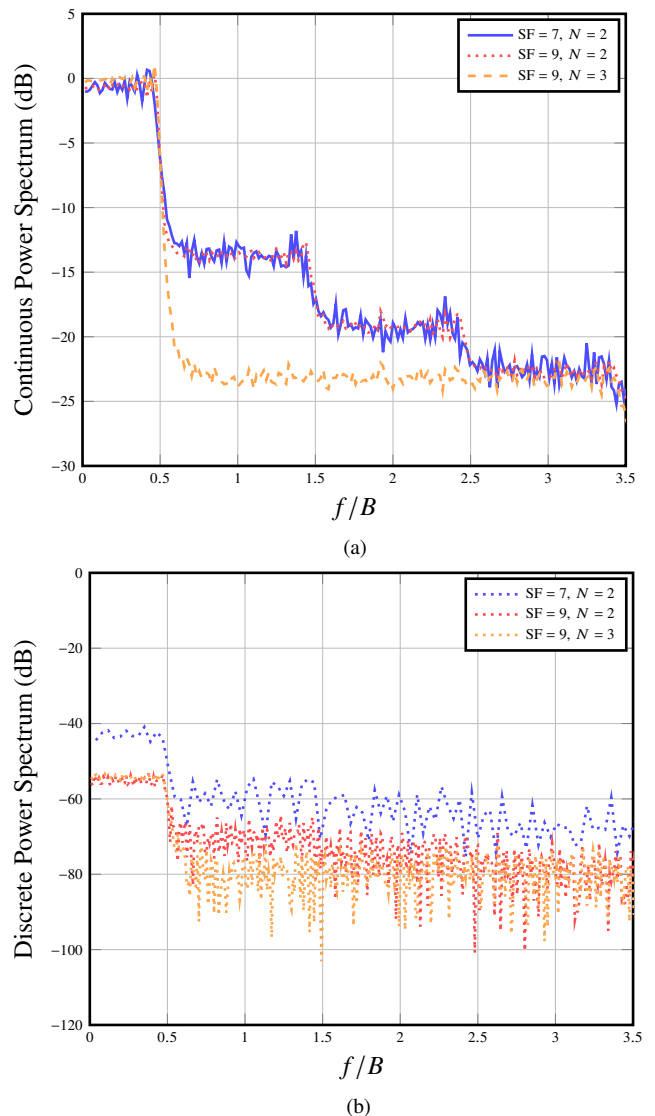


Fig. 5: Continuous and discrete spectrum of baseband LoRa backscatter signals with  $SF \in \{7, 9\}$  and  $N \in \{2, 3\}$ : (a) continuous part of the spectrum, (b) discrete spectrum.

## V. NUMERICAL RESULTS AND DISCUSSION

In this section, we show the performance of LB in terms of the power spectrum and error performance in AWGN and fading channels.

### A. Power Spectrum

In Fig. 5, we present the double-sided power spectrum of the baseband LB signals as a function of normalized frequency  $f/B$  with different spreading factors and the number of phases, i.e.,  $SF \in \{7, 9\}$  and  $N \in \{2, 3\}$ . We only show  $\mathcal{G}_I(f)$  for  $f \geq 0$  because  $\mathcal{G}_I(f) = \mathcal{G}_I(-f)$ . We show both the normalized power spectral density,  $10 \log(\mathcal{G}_I^{(c)}(f) * B)$ , and the discrete part of the spectrum. For the discrete spectrum, we show the power  $\left| \sum_{a=0}^{M-1} S_a \left(\frac{lB}{M}\right) \right|^2 / M^2 T_s^2$  at frequency  $lB/M$ . We see from the continuous part of the spectrum that it has a staircase shape where the power spectrum does not always

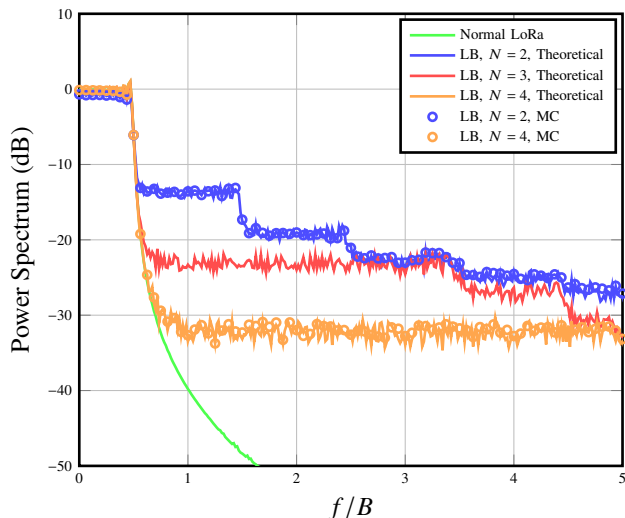


Fig. 6: Power Spectrum of baseband LoRa and LoRa backscatter modulated signals at SF = 9 for  $N \in \{2, 3, 4\}$ .

decrease as frequency increases but maintains relatively stable over some frequency ranges. Also, for a higher number of phases, i.e., loads, the spectrum drops faster compared to that with a smaller number of quantization phases. We can also see that as SF increases, the power spectrum gets increasingly condensed so that more power of the complex envelope is contained between  $-B/2$  and  $B/2$ .

In Fig. 6, we compare the derived total power spectrum with both continuous and discrete parts with that of normal LoRa at SF = 9, for various numbers of quantization phases, i.e.,  $N \in \{2, 3, 4\}$ . The frequency range of interest is split into multiple bins of  $\Delta f = B/1024$  width. We verified the analytical results using Monte Carlo simulations generated by estimating the power spectral density in (15) using Welch's method. Only the cases for  $N \in \{2, 4\}$  are included for space limitation. We see from the figure that the power spectrum of LB modulated signals has a strong similarity with that of normal LoRa in the range of  $f \in [0, B/2]$ . However, the power spectrum of LB signals begins to saturate for  $f > B/2$  while that of normal LoRa decreases continuously. For an increasing number of phases, LB matches normal LoRa for a larger frequency range. For example, at  $f/B = 1$ , the power spectrum of LB with  $N = 5$  is nearly equivalent to normal LoRa, while for  $N = 2$ , the gap is approximately over 25 dB.

Also, we investigate the LB spectrum in the ISM band with the ETSI regulations [41]. In Fig. 7, we report the one-sided power spectrum calculated with SF = 7, the resolution bandwidth RBW = 1 kHz and transmission power  $P_s = 14$  dBm, i.e., the maximum allowed power. The spectrum exceeds the spectral mask for  $N = 3$  while it is within the mask for  $N = 4$  at the maximum transmission power. Thus, to satisfy the ETSI regulation on the ISM band, one should either increase the number of loads used in the tag or decrease the transmission power. The same approach may be used to investigate the compliance of LB for different ISM bands, spreading factors, number of quantization phases, and bandwidths in accordance with other regional requirements.

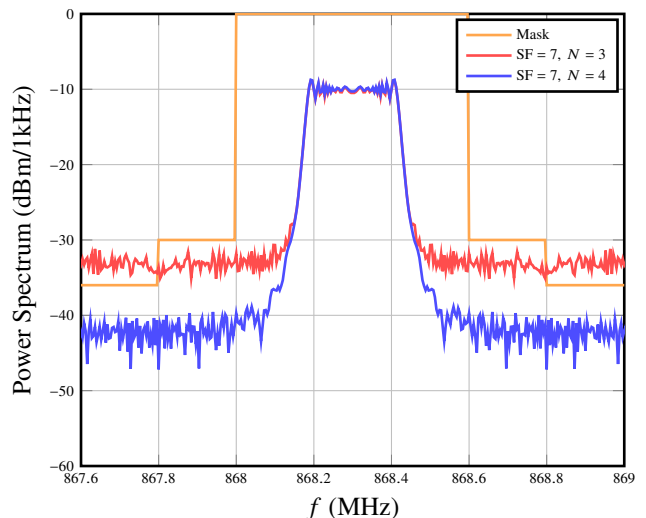


Fig. 7: One-sided power spectrum for LoRa backscatter pass-band signals compared with the mask of the ETSI regulation in the G1 sub-band, for SF = 7,  $N \in \{3, 4\}$ ,  $B = 250$  kHz, RBW=1 kHz and  $P_s = 14$  dBm.

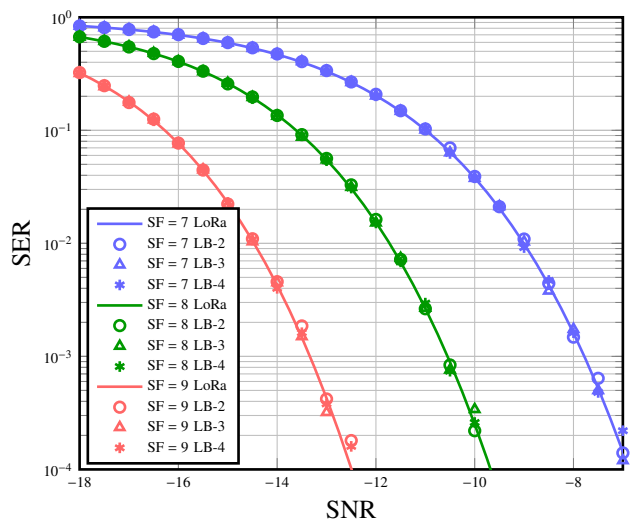


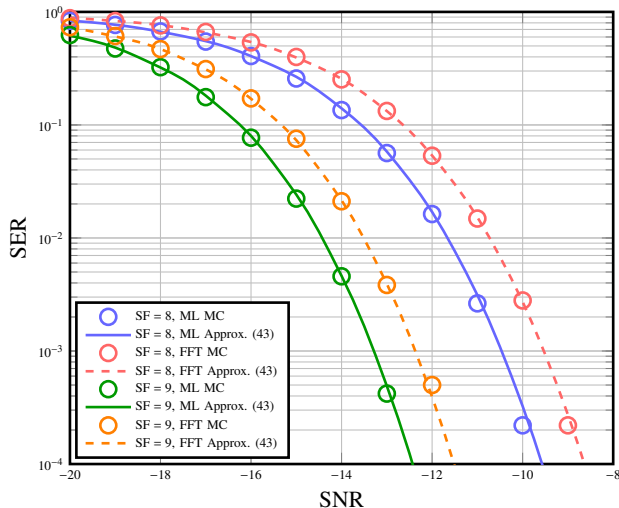
Fig. 8: The SER performance in the AWGN channel using ML decoder at SF  $\in \{7, 8, 9\}$  of normal LoRa and LB for  $N \in \{2, 3, 4\}$ .

### B. Error Performance in AWGN Channels

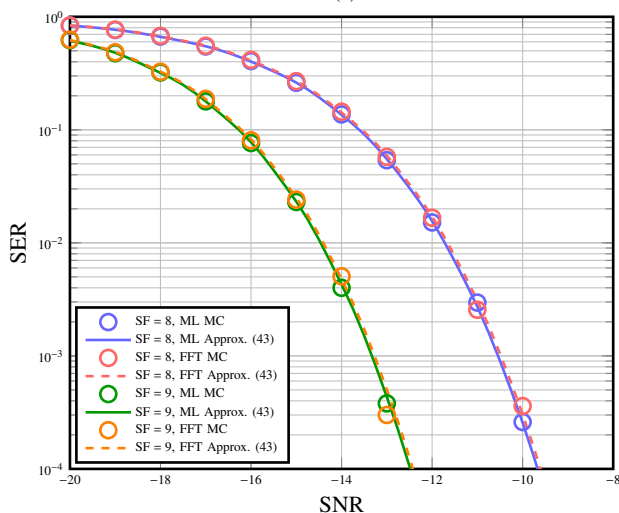
In Fig. 8, we compare the SER using ML decoder in the AWGN channel at SF  $\in \{7, 8, 9\}$  for normal LoRa and LB with the different number of quantization phases, where, as a benchmark, the curves for normal LoRa are calculated by computing integrals numerically:

$$\int_0^\infty \left[ 1 - \left[ 1 - \exp \left[ -\frac{l^2}{2\sigma^2} \right] \right]^{M-1} \right] f_{\mathcal{L}_{(a,a)}^{\text{ML}}}(l) dl, \quad (70)$$

and the curves for LB are from Monte Carlo simulation. It can be observed that the SER for LB using ML decoder has a strong similarity to normal LoRa for various values of the SFs and number of loads, even though the LB waveforms are non-



(a)



(b)

Fig. 9: LB SER performance in the AWGN channel at SF=8,9: (a)  $N = 2$ , (b)  $N = 4$ .

orthogonal. We verified the results for small lower values of SF and still find the error performance similar to each other. The results suggest that existing works discussing the error performance of orthogonal LoRa can be also applied to LB using ML when considering detectors.

Fig. 9 presents comparisons of derived LB SER approximation in (43) with the theoretical SER calculated by numerically computing the integral in (33) at SF = 8,9 in the AWGN channel. The figures also include the results from the Monte Carlo simulation. As shown in the figure, the derived expression in (43) exhibits a tight approximation to the theoretical results. Furthermore, comparing the SER using ML and FFT decoders, the SER gap between them differs hugely depending on the number of quantization phases. Improved SER using FFT decoder is evident when increasing  $N$ . While the gap is around 1 dB at SER of  $10^{-3}$  for SF = 9 when using only 4 quantization phases, there are nearly no differences between the performance of two decoders with 16 quantization phases, indicating that the error performance with  $N \geq 4$  is similar to

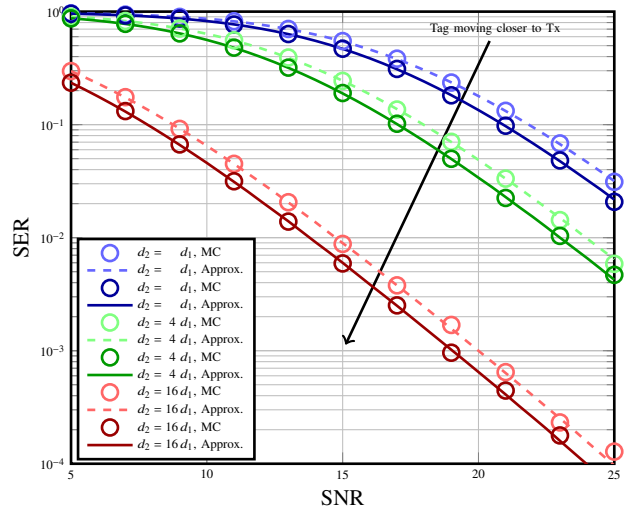


Fig. 10: LB SER performance in double Nakagami-m fading channels using ML decoder for SF = 7 and  $N = 2$  (dashed),  $N = 4$  (solid).

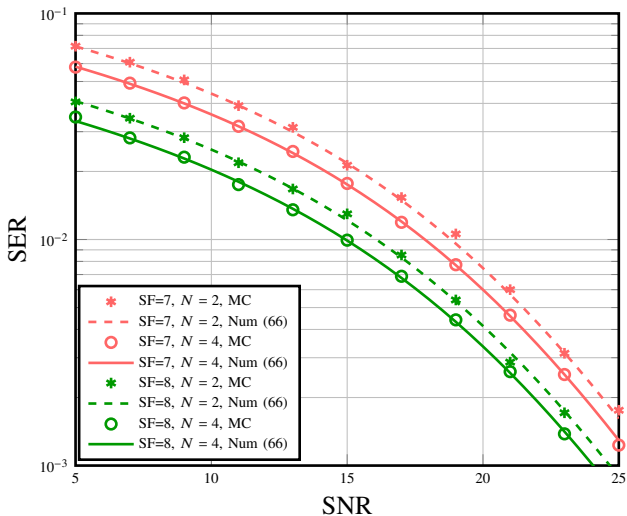


Fig. 11: SER performance for LB with water-filling technique using FFT decoder at SF  $\in \{7, 8\}$  and  $N \in \{2, 4\}$ .

orthogonal LoRa for both ML and FFT detectors in AWGN channel.

### C. Error Performance in Fading Channels With Fixed Transmit Power and Limited Average Power

In Fig. 10, we plot the SER performance of LB over double Nakagami-m fading channels at SF = 7 and  $N = 2, 4$  where we fix the total distance of the reflected path between the Tx and Rx through the tag, i.e.,  $d = d_1 + d_2$ . In addition, we consider a path loss model where the energy is inversely proportional to the squared distance, i.e.,  $\mathbb{V}[|h_1|] \propto 1/d_1^2$  and  $\mathbb{V}[|h_2|] \propto 1/d_2^2$ . In this simulation, we consider the FFT decoder. It is shown that a better SER performance is achieved when the tag is placed closer to the Tx, which is similar to the experimental results in [15]. Also, the comparison of the derived SER approximation (62) to the curves calculated by

numerical integrating (47) and the Monte Carlo simulation presents an accurate approximation.

On the other hand, for the model with limited average power, we show the error performance of LB with a water-filling power allocation scheme in Fig. 11 using FFT decoder at  $SF \in \{7, 8\}$  and  $N \in \{2, 4\}$ . The theoretical curves from numerical integrating (66) are consistent with the Monte Carlo simulations.

## VI. CONCLUSION

In this paper, we provide the first mathematical expression of LB signals with a finite number of loads. Based on the expression, we derived the closed-form expressions for the power spectrum of LB, showing the staircase-shaped spectrum. To satisfy the wireless transmission regulations, measures such as increasing the number of phases or decreasing the transmit power may be needed. An analytical approximation of SER for LB in both AWGN and double Nakagami- $m$  fading channels using two different decoders is derived. The results suggest that the SER performance of LB using ML decoder with a small number of phases is similar to LoRa modulation, while the SER performance using FFT decoder is worse. On the other hand, SER performance using FFT decoder will improve with more quantization phases. In the double fading scenarios, a longer communication range can be achieved by setting the backscatter tag closer to Tx.

### APPENDIX A

#### PROOF THAT MAXIMUM LIKELIHOOD DECODER IS OPTIMUM FOR LORA BACKSCATTER

The Tx sends the real part of the passband signal with symbol  $a$  to the Rx:

$$R(t) = \text{Re} [r_a(t) e^{j2\pi f_c t}], \quad (71)$$

where  $r_a(t) = |h| \sqrt{E_s} x_a(t) e^{j\theta_h} + \omega(t)$  is the corresponding baseband signal,  $\theta_h$  is the phase of complex channel gain  $h$ , and  $f_c$  is the carrier frequency. We assume that the channel amplitude  $|h|$  and the delay  $\tau$  are known to Rx. The symbol decision is based on choosing the maximum among a set of posteriori probabilities [55]

$$\hat{a} = \arg \max_{0 \leq a \leq M-1} P_a p(R(t) | x_a(t), |h|, \tau) \quad (72)$$

$$= \arg \max_{0 \leq a \leq M-1} \int_0^{2\pi} p(R(t) | x_a(t), |h|, \tau, \theta_h) p(\theta_h) d\theta_h,$$

where  $P_a$  is the probability of transmitting symbol  $a$ ,  $p(\theta_h)$  is the PDF of  $\theta_h$ . We consider equiprobable transmit symbols and uniformly distributed phases as is typical for Rayleigh, Rician, and Nakagami fading channels. The probability  $p(R(t) | x_a(t), |h|, \tau, \theta_h)$  is a joint Gaussian PDF

$$p(R(t) | x_a(t), |h|, \tau, \theta_h) = K \exp \left( \text{Re} \left\{ \frac{|h|}{N_0} e^{-j\theta_h} y_a(\tau) \right\} - \frac{|h|^2 E_a}{N_0} \right), \quad (73)$$

where  $K$  is an integral constant and

$$y_a(\tau) = \int_0^{T_s} r_a(t + \tau) x_a^*(t) dt \quad (74)$$

is the complex correlation of the received signal and the signal waveform of symbol  $a$  and

$$E_a = \frac{1}{2} \int_0^{T_s} |x_a(t)|^2 dt \quad (75)$$

is the energy of the waveform  $x_a(t)$ . Thus, we obtain

$$p(R(t) | x_a(t), |h|, \tau) = \exp \left( -\frac{|h|^2 E_a}{N_0} \right) \frac{K}{2\pi} \int_0^{2\pi} \exp \left( \text{Re} \left\{ \frac{|h|}{N_0} e^{-j\theta_h} y_a(\tau) \right\} \right) d\theta_h. \quad (76)$$

Substitute (76) into (72) and remove the terms that are independent of  $a$ , we obtain

$$\begin{aligned} \hat{a} &= \arg \max_{0 \leq a \leq M-1} \int_0^{2\pi} \exp \left( \text{Re} \left\{ e^{-j\theta_h} y_a(\tau) \right\} \right) d\theta_h \\ &= \arg \max_{0 \leq a \leq M-1} \int_0^{2\pi} \exp (|y_a(\tau)| \cos [\theta_h - \arg (y_a(\tau))]) d\theta_h \\ &= \arg \max_{0 \leq a \leq M-1} I_0 (|y_a(\tau)|), \end{aligned} \quad (77)$$

where the term  $E_a$  is independent of  $a$  because the waveforms of different symbols have the same energy. Since  $I_0$  is a monotonically increasing function, the optimum decision is made by choosing the symbol that has the maximum cross-correlation with the received signal.

### APPENDIX B

#### HOW TO OBTAIN $\{t_m\}_{m=1}^{\psi}$

$t_m$  are times when the value of  $\tilde{Q}_N [f(t)]$  make discrete changes. The set of  $t_m$  can be obtained by solving

$$f(t) = \frac{i\pi}{2^{N-1}}, \quad i \in \mathbb{Z}, \quad t \in [0, M/B], \quad (78)$$

where the two parts of  $f(t)$  are quadratic functions so that the roots can be easily obtained. It is feasible to directly solve  $f_1(t) = i\pi/2^{N-1}$  and  $f_2(t) = i\pi/2^{N-1}$  individually in their respective regions. However, it is worth noting that we have the equality

$$f_2(t) = f_1 \left( t - \frac{M}{B} \right). \quad (79)$$

We see that  $f_2(t)$  is a shifted version of  $f_1(t)$ , which can be leveraged to simplify the solution. More precisely, the roots of  $f_2(t) = i\pi/2^{N-1}$  in the region  $\frac{M-a}{B} \leq t \leq \frac{M}{B}$  are corresponding to the roots of  $f_1(t) = i\pi/2^{N-1}$  in region  $-\frac{a}{B} \leq t \leq 0$ . Hence, all the roots can be obtained by calculating the roots of  $f_1(t) = i\pi/2^{N-1}$  for  $t \in [-\frac{a}{B}, \frac{M-a}{B}]$  using root formula for quadratic equation

$$z_i^\pm = \frac{(M-2a) \pm \sqrt{(M-2a)^2 + iM2^{3-N}}}{2B}, \quad \left[ -\frac{(M-2a)^2}{2^{3-n}M} \right] \leq i \leq \left\lfloor \frac{a(M-a)}{2^{1-n}M} \right\rfloor. \quad (80)$$

Next, add  $M/B$  to  $z_i^\pm$  if they are negative. Also,  $t = M/B$  should be added to the roots set because it overlaps with root  $t = 0$  before being shifted. Finally, rearrange all roots from smallest to largest, namely,  $t_1 \leq t_2 \leq \dots \leq t_\psi$ .

## APPENDIX C

PROOF THAT  $\mathcal{L}_{(a,i)}^D$  FOLLOW RICIEN DISTRIBUTION WITH

$$\text{SHAPE PARAMETER } \kappa_{(a,i)}^D = \frac{|h\sqrt{E_s}\xi_{(a,i)}^D|^2}{2\sigma^2}$$

The Rician distribution is the probability distribution of the magnitude of a circularly-symmetric bivariate normal random variable. A r.v.  $\mathcal{L} = \sqrt{\mathcal{X}^2 + \mathcal{Y}^2}$  follows the Rician distribution with shape parameter  $\kappa = |\nu|^2/2\sigma^2$  if  $\mathcal{X} \sim \mathcal{N}(\nu \sin \theta, \sigma^2)$  and  $\mathcal{Y} \sim \mathcal{N}(\nu \cos \theta, \sigma^2)$ , where  $\mathcal{X}$  and  $\mathcal{Y}$  are independently distributed normal r.v.s and  $\theta = \nu/|\nu|$ .  $\mathcal{L}_{(a,i)}^D$  is the amplitude of a complex r.v.

$$\mathcal{L}_{(a,i)}^D = \left| h\sqrt{E_s}\xi_{(a,i)}^D + \mathcal{W}_{(a,i)}^D \right| \quad (81)$$

$$= \left| \left| h\sqrt{E_s}\xi_{(a,i)}^D \right| e^{j\beta} e^{-j\beta} + \mathcal{W}_{(a,i)}^D e^{-j\beta} \right|, \quad (82)$$

where  $e^{j\beta}$  is the angle of  $h\sqrt{E_s}\xi_{(a,i)}^D$ , and the second term is the rotated version of complex Gaussian r.v.. Thus, we define

$$\mathcal{X} = \left| h\sqrt{E_s}\xi_{(a,i)}^D \right| + \text{Re} \left[ \mathcal{W}_{(a,i)}^D e^{-j\beta} \right], \quad (83)$$

$$\mathcal{Y} = \text{Im} \left[ \mathcal{W}_{(a,i)}^D e^{-j\beta} \right], \quad (84)$$

where  $\mathcal{L}_{(a,i)}^D = |\mathcal{X} + j\mathcal{Y}|$ . Since  $\mathcal{X} \sim \mathcal{N} \left( \left| h\sqrt{E_s}\xi_{(a,i)}^D \right|, \sigma^2 \right)$  and  $\mathcal{Y} \sim \mathcal{N} (0, \sigma^2)$ ,  $\mathcal{L}_{(a,i)}^D$  follows Rician distribution with shape parameter  $\kappa_{(a,i)}^D = \frac{|h\sqrt{E_s}\xi_{(a,i)}^D|^2}{2\sigma^2}$ .

## REFERENCES

- [1] F. Boccardi, R. W. Heath, A. Lozano, T. L. Marzetta, and P. Popovski, "Five disruptive technology directions for 5G," *IEEE Communications Magazine*, vol. 52, no. 2, pp. 74–80, Feb. 2014.
- [2] S. Dang, O. Amin, B. Shihada, and M.-S. Alouini, "What should 6G be?" *Nature Electronics*, vol. 3, no. 1, pp. 20–29, 2020.
- [3] L. S. Vailshery, "Iot connected devices worldwide 2019-2030," Jun 2022. [Online]. Available: <https://www.statista.com/statistics/1183457/iot-connected-devices-worldwide/>
- [4] M. Chiani and A. Elzanaty, "On the LoRa modulation for IoT: Waveform properties and spectral analysis," *IEEE Internet of Things Journal*, vol. 6, no. 5, pp. 8463–8470, Oct. 2019.
- [5] U. Raza, P. Kulkarni, and M. Sooriyabandara, "Low power wide area networks: An overview," *IEEE Communications Surveys & Tutorials*, vol. 19, no. 2, pp. 855–873, Secondquarter 2017.
- [6] D. Pianini, A. Elzanaty, A. Giorgetti, and M. Chiani, "Emerging distributed programming paradigm for cyber-physical systems over LoRAWANs," in *2018 IEEE Globecom Workshops (GC Wkshps)*, Dec. 2018, pp. 1–6.
- [7] S. Sobhi, A. Elzanaty, M. Y. Selim, A. M. Ghuniem, and M. F. Abdelkader, "Mobility of LoRaWAN gateways for efficient environmental monitoring in pristine sites," *Sensors*, vol. 23, no. 3, 2023. [Online]. Available: <https://www.mdpi.com/1424-8220/23/3/1698>
- [8] F. Rezaei, C. Tellambura, and S. Herath, "Large-scale wireless-powered networks with backscatter communications—a comprehensive survey," *IEEE Open Journal of the Communications Society*, vol. 1, pp. 1100–1130, July 2020.
- [9] C. Song, Y. Ding, A. Eid, J. G. D. Hester, X. He, R. Bahr, A. Georgiadis, G. Goussetis, and M. M. Tentzeris, "Advances in wirelessly powered backscatter communications: From antenna/RF circuitry design to printed flexible electronics," *Proceedings of the IEEE*, vol. 110, no. 1, pp. 171–192, Jan. 2022.
- [10] N. Van Huynh, D. T. Hoang, X. Lu, D. Niyato, P. Wang, and D. I. Kim, "Ambient backscatter communications: A contemporary survey," *IEEE Communications Surveys & Tutorials*, vol. 20, no. 4, pp. 2889–2922, May 2018.
- [11] G. Wang, F. Gao, R. Fan, and C. Tellambura, "Ambient backscatter communication systems: Detection and performance analysis," *IEEE Transactions on Communications*, vol. 64, no. 11, pp. 4836–4846, Nov. 2016.
- [12] V. Liu, A. Parks, V. Talla, S. Gollakota, D. Wetherall, and J. R. Smith, "Ambient backscatter: Wireless communication out of thin air," *ACM SIGCOMM Computer Communication Review*, vol. 43, no. 4, pp. 39–50, Oct. 2013.
- [13] Y. H. Al-Badarnah, A. Elzanaty, and M.-S. Alouini, "On the performance of spectrum-sharing backscatter communication systems," *IEEE Internet of Things Journal*, vol. 9, no. 3, pp. 1951–1961, Feb. 2022.
- [14] V. Iyer, V. Talla, B. Kellogg, S. Gollakota, and J. Smith, "Inter-technology backscatter: Towards internet connectivity for implanted devices," in *Proceedings of the 2016 ACM SIGCOMM Conference*, ser. SIGCOMM '16. New York, NY, USA: Association for Computing Machinery, Aug. 2016, p. 356–369.
- [15] V. Talla, M. Hesar, B. Kellogg, A. Najafi, J. R. Smith, and S. Gollakota, "LoRa backscatter: Enabling the vision of ubiquitous connectivity," *Proceedings of the ACM on Interactive, Mobile, Wearable and Ubiquitous Technologies*, vol. 1, no. 3, pp. 1–24, Sept. 2017.
- [16] X. Tang, G. Xie, and Y. Cui, "Self-sustainable long-range backscattering communication using RF energy harvesting," *IEEE Internet of Things Journal*, vol. 8, no. 17, pp. 13 737–13 749, Sept. 2021.
- [17] M. Katanbaf, A. Weinand, and V. Talla, "Simplifying backscatter deployment: Full-duplex LoRa backscatter," in *18th USENIX Symposium on Networked Systems Design and Implementation (NSDI 21)*, 2021, pp. 955–972.
- [18] H. Li, X. Tong, Q. Li, and X. Tian, "XORLoRa: LoRa backscatter communication with commodity devices," in *2020 IEEE 6th International Conference on Computer and Communications (ICCC)*, Dec. 2020, pp. 706–711.
- [19] Y. Peng, L. Shangguan, Y. Hu, Y. Qian, X. Lin, X. Chen, D. Fang, and K. Jamieson, "Plora: A passive long-range data network from ambient LoRa transmissions," in *Proceedings of the 2018 Conference of the ACM Special Interest Group on Data Communication*, 2018, pp. 147–160.
- [20] G. Huang, P. Yang, H. Zhou, Y. Yan, X. He, and X. Li, "Freeback: Blind and distributed rate adaptation in LoRa-based backscatter networks," in *2021 IEEE Wireless Communications and Networking Conference (WCNC)*, Mar.-Apr. 2021, pp. 1–6.
- [21] X. Guo, L. Shangguan, Y. He, J. Zhang, H. Jiang, A. A. Siddiqi, and Y. Liu, "Efficient ambient LoRa backscatter with on-off keying modulation," *IEEE/ACM Transactions on Networking*, pp. 1–14, Nov. 2021.
- [22] M. Lazaro, A. Lazaro, and R. Villarino, "Feasibility of backscatter communication using LoRAWAN signals for deep implanted devices and wearable applications," *Sensors*, vol. 20, no. 21, p. 6342, Nov. 2020.
- [23] N. Fasarakis-Hilliard, P. N. Alevizos, and A. Bletsas, "Coherent detection and channel coding for bistatic scatter radio sensor networking," *IEEE Transactions on Communications*, vol. 63, no. 5, pp. 1798–1810, May 2015.
- [24] J. Qian, F. Gao, G. Wang, S. Jin, and H. Zhu, "Noncoherent detections for ambient backscatter system," *IEEE Transactions on Wireless Communications*, vol. 16, no. 3, pp. 1412–1422, march 2017.
- [25] J. K. Devineni and H. S. Dhillon, "Ambient backscatter systems: Exact average bit error rate under fading channels," *IEEE Transactions on Green Communications and Networking*, vol. 3, no. 1, pp. 11–25, March 2019.
- [26] J. Qian, Y. Zhu, C. He, F. Gao, and S. Jin, "Achievable rate and capacity analysis for ambient backscatter communications," *IEEE Transactions on Communications*, vol. 67, no. 9, pp. 6299–6310, Sept. 2019.
- [27] G. Ferré and A. Giremus, "LoRa physical layer principle and performance analysis," in *2018 25th IEEE International Conference on Electronics, Circuits and Systems (ICECS)*, Dec. 2018, pp. 65–68.
- [28] J. G. Proakis and M. Salehi, *Digital Communications*, 5th ed. New York, NY, USA: McGraw-Hill, 2007.
- [29] C. Ferreira Dias, E. Rodrigues de Lima, and G. Fraidenraich, "Bit error rate closed-form expressions for LoRa systems under Nakagami and Rice fading channels," *Sensors*, vol. 19, no. 20, p. 4412, Oct. 2019.
- [30] V. Savaux and G. Ferré, "Simple asymptotic BER expressions for LoRa system over Rice and Rayleigh channels," in *2021 Wireless Telecommunications Symposium (WTS)*, Apr. 2021, pp. 1–4.
- [31] T. Elshabrawy and J. Robert, "Closed-form approximation of LoRa modulation BER performance," *IEEE Communications Letters*, vol. 22, no. 9, pp. 1778–1781, Sept. 2018.
- [32] J. Courjault, B. Vrigneau, O. Berder, and M. R. Bhatnagar, "A computable form for LoRa performance estimation: Application to Ricean and Nakagami fading," *IEEE Access*, vol. 9, pp. 81 601–81 611, Apr. 2021.
- [33] G. Baruffa, L. Rugini, L. Germani, and F. Frescura, "Error probability performance of chirp modulation in uncoded and coded lora systems," *Digital Signal Processing*, vol. 106, p. 102828, Nov. 2020.

- [34] S. An, H. Wang, Y. Sun, Z. Lu, and Q. Yu, "Time domain multiplexed lora modulation waveform design for iot communication," *IEEE Communications Letters*, vol. 26, no. 4, pp. 838–842, April 2022.
- [35] M. J. Faber, K. M. van der Zwaag, W. G. V. dos Santos, H. R. d. O. Rocha, M. E. V. Segatto, and J. A. L. Silva, "A theoretical and experimental evaluation on the performance of LoRa technology," *IEEE Sensors Journal*, vol. 20, no. 16, pp. 9480–9489, Aug. 2020.
- [36] O. Afsiadis, M. Cotting, A. Burg, and A. Balatsoukas-Stimming, "On the error rate of the LoRa modulation with interference," *IEEE Transactions on Wireless Communications*, vol. 19, no. 2, pp. 1292–1304, Feb. 2020.
- [37] T. Elshabrawy and J. Robert, "Analysis of BER and coverage performance of LoRa modulation under same spreading factor interference," in *2018 IEEE 29th Annual International Symposium on Personal, Indoor and Mobile Radio Communications (PIMRC)*, Sept. 2018, pp. 1–6.
- [38] D. Croce, M. Gucciardo, S. Mangione, G. Santaromita, and I. Tinnirello, "Impact of LoRa imperfect orthogonality: Analysis of link-level performance," *IEEE Communications Letters*, vol. 22, no. 4, pp. 796–799, Apr. 2018.
- [39] F. Benkhelifa, Y. Bouazizi, and J. A. McCann, "How orthogonal is LoRa modulation?" *IEEE Internet of Things Journal*, vol. 9, no. 20, pp. 19928–19944, May 2022.
- [40] A. S. Ali, L. Bariah, S. Muhaidat, P. Sofotasios, and M. Al-Qutayri, "Performance analysis of LoRa-backscatter communication system in awgn channels," in *2021 4th International Conference on Advanced Communication Technologies and Networking (CommNet)*, Dec. 2021, pp. 1–5.
- [41] "Electromagnetic compatibility and radio spectrum matters (ERM); shortrange devices (SRD); radio equipment to be used in the 25 mhz to 1000 mhz frequency range with power levels ranging up to 500 mw; part 1: Technical characteristics and test methods," Eur. Telecommun. Stand. Inst., Sophia Antipolis, France, Standard, 2012.
- [42] J. W. Harris and H. Stöcker, *Handbook of mathematics and computational science*. Springer Science & Business Media, 1998.
- [43] T. Elshabrawy, P. Edward, M. Ashour, and J. Robert, "On the different mathematical realizations for the digital synthesis of lora-based modulation," in *European Wireless 2019; 25th European Wireless Conference*, May 2019, pp. 1–6.
- [44] E. A. Lee and D. G. Messerschmitt, *Digital communication*. Springer Science & Business Media, 2012.
- [45] S. Benedetto and E. Biglieri, *Principles of digital transmission: with wireless applications*. Springer Science & Business Media, 1999.
- [46] M. Simon and M. Alouini, "A unified approach to the performance analysis of digital communication over generalized fading channels," *Proceedings of the IEEE*, vol. 86, no. 9, pp. 1860–1877, 1998.
- [47] M. Abramowitz and I. A. Stegun, *Handbook of mathematical functions with formulas, graphs, and mathematical tables*. US Government printing office, 1964, vol. 55.
- [48] H. Gudbjartsson and S. Patz, "The Rician distribution of noisy MRI data," *Magnetic resonance in medicine*, vol. 34, no. 6, pp. 910–914, 1995.
- [49] A. Subhash, S. Kalyani, Y. H. Al-Badarneh, and M.-S. Alouini, "On the asymptotic performance analysis of the k-th best link selection over non-identical non-central chi-square fading channels," *IEEE Transactions on Communications*, vol. 70, no. 11, pp. 7191–7206, Nov. 2022.
- [50] G. K. Karagiannidis, N. C. Sagias, and P. T. Mathiopoulos, "N\*Nakagami: A novel stochastic model for cascaded fading channels," *IEEE Transactions on Communications*, vol. 55, no. 8, pp. 1453–1458, Aug. 2007.
- [51] I. S. Gradshteyn and I. M. Ryzhik, *Table of integrals, series, and products*. Academic press, 2014.
- [52] P. Rabinowitz and G. Weiss, "Tables of abscissas and weights for numerical evaluation of integrals of the form  $\int_0^\infty e^{-x} x^n f(x) dx$ ," *Mathematical Tables and Other Aids to Computation*, pp. 285–294, 1959.
- [53] Z.-H. Yang and S.-Z. Zheng, "The monotonicity and convexity for the ratios of modified Bessel functions of the second kind and applications," *Proceedings of the American Mathematical Society*, vol. 145, no. 7, pp. 2943–2958, Jan. 2017.
- [54] A. Goldsmith, *Wireless communications*. Cambridge university press, 2005.
- [55] M. K. Simon and M.-S. Alouini, *Digital communication over fading channels*. John Wiley & Sons, 2005, vol. 95.